

# Difference image photometry with bright variable backgrounds

E. Kerins,<sup>1</sup> M.J. Darnley,<sup>2</sup> J.P. Duke,<sup>2</sup> A. Gould,<sup>3</sup> C. Han,<sup>4</sup> A. Newsam,<sup>2</sup>  
B.-G. Park<sup>5</sup> and R. Street<sup>6</sup>

<sup>1</sup>*Jodrell Bank Centre for Astrophysics, School of Physics & Astronomy, University of Manchester, Oxford Road, Manchester M13 9PL*

<sup>2</sup>*Astrophysics Research Institute, Liverpool John Moores University, Twelve Quays House, Egerton Wharf, Birkenhead, Merseyside CH41 1LD*

<sup>3</sup>*Department of Astronomy, Ohio State University, 140 West 18th Avenue, Columbus, OH 43210, USA*

<sup>4</sup>*Department of Physics, Chungbuk National University, Chongju 361-763, Korea*

<sup>5</sup>*Korea Astronomy and Space Science Institute, Hwaam-Dong, Yuseong-Gu, Daejeon 305-348, Korea*

<sup>6</sup>*Las Cumbres Observatory Global Telescope Network, 6740 Cortona Drive, Suite 102, Goleta, CA 93117, USA*

6 July 2010

## ABSTRACT

Over the last two decades the Andromeda Galaxy (M31) has been something of a test-bed for methods aimed at obtaining accurate time-domain relative photometry within highly crowded fields. Difference imaging methods, originally pioneered towards M31, have evolved into sophisticated methods, such as the Optimal Image Subtraction (OIS) method of Alard & Lupton (1998), that today are most widely used to survey variable stars, transients and microlensing events in our own Galaxy. We show that modern difference image (DIA) algorithms such as OIS, whilst spectacularly successful towards the Milky Way bulge, may perform badly towards high surface brightness targets such as the M31 bulge. Poor results can occur in the presence of common systematics which add spurious flux contributions to images, such as internal reflections, scattered light or fringing. Using data from the Angstrom Project microlensing survey of the M31 bulge, we show that very good results are usually obtainable by first performing careful photometric alignment prior to using OIS to perform point-spread function (PSF) matching. This separation of background matching and PSF matching, a common feature of earlier M31 photometry techniques, allows us to take full advantage of the powerful PSF matching flexibility offered by OIS towards high surface brightness targets. We find that difference images produced this way have noise distributions close to Gaussian, showing significant improvement upon results achieved using OIS alone. We show that with this correction light-curves of variable stars and transients can be recovered to within  $\sim 10$  arcseconds of the M31 nucleus. Our method is simple to implement and is quick enough to be incorporated within real-time DIA pipelines. We also demonstrate that OIS is remarkably robust even when, as in the case of the central regions of the M31 bulge, the sky density of variable sources approaches the confusion limit.

**Key words:** galaxies: individual (M31) – techniques: image processing – techniques: photometric

## 1 INTRODUCTION

Difference Image Analysis (DIA) is now used routinely to provide very accurate relative photometry of variable stars, transient objects and microlensing events in the Milky Way and other nearby galaxies (Wozniak 2008). DIA permits very accurate relative photometry even within extremely dense stellar fields where conventional photometric methods can fail or suffer from serious bias.

Most DIA pipelines currently in use derive from the Optimal Image Subtraction (OIS) algorithm of Alard & Lupton (1998) and Alard (2000). The OIS algorithm has found widest use in providing accurate relative photometry of stars in the Milky Way and the Magellanic Clouds. Similar schemes that pre-date OIS were originally employed to look for microlensing towards the Andromeda

Galaxy (Tomaney & Crotts 1996; Ansari et al. 1997). Since the stars in the Andromeda Galaxy (M31) are two orders of magnitude further away than those typically monitored in our Galaxy, difference imaging towards M31 throws up several additional challenges to the standard technique.

In this paper we show that towards the bulge of M31, and similarly towards other targets where diffuse background surface brightness dominates the total flux, DIA pipelines based on the OIS algorithm can often yield poor results due to common image systematics such as internal reflections, scattered light or fringe effects. Systematics, which may appear at a low level ( $\sim 1\%$ ) on the original exposures, can give rise to large-amplitude differential background residuals on difference image frames. Since OIS minimizes mismatches in both the point spread function (PSF) and the

differential background simultaneously, poor background matching often results in poor PSF matching and therefore substantial systematic errors in differential photometry. We propose a straightforward remedy to allow the effects of such systematics to be minimized.

The structure of the paper is as follows. In Section 2 we briefly describe how M31 has been used as a test-bed in developing time-domain photometry towards crowded stellar fields. The evolution of these methods culminated in the Optimal Image Subtraction (OIS) algorithm of Alard & Lupton (1998) and Alard (2000), which forms the basis for most DIA pipelines currently in use. We use images obtained by the Angstrom Project (Kerins et al. 2006) of the bulge region of M31 to show how the OIS algorithm may not perform optimally in the presence of bright backgrounds. In Section 3 we show how difference images with noise levels close to the photon noise limit can be recovered by separating the photometric alignment and PSF matching stages. In Section 4 we show some example periodic variable light-curves from the Angstrom Project dataset, illustrating the impact of the correction on their photometric quality and on the ability to characterise variable stars at a range of distances from the M31 core. We discuss the findings in Section 5.

## 2 DIFFERENCE IMAGING TOWARDS THE M31 BULGE

### 2.1 Relative photometry in very crowded fields

The Andromeda Galaxy has provided something of a test-bed for the development of algorithms designed to obtain accurate relative photometry within crowded fields. At around the same time two techniques emerged, difference imaging (Tomaney & Crotts 1996) and super-pixel photometry (Ansari et al. 1997). Both techniques deal with the difficulty of obtaining robust relative photometry across epochs in the presence of variations in seeing and sky background.

Tomaney & Crotts (1996) advocated the difference imaging approach, in which they convolve a high quality reference image with a Gaussian kernel to match the point spread function (PSF) of a target image. Prior to the convolution step the smooth M31 background light was subtracted from both images using a local median filter. The PSF matching approach forms the basis of most current difference imaging codes, though it assumes the basic functional form of the PSF is known a priori. Modern implementations do not include a separate background subtraction stage but instead solve for the PSF and background simultaneously.

In the super-pixels method (Ansari et al. 1997) an image pair is also photometrically aligned in order to match the background levels. This was done first through linear photometric alignment and then by local median filtering the images to produce smooth background maps. The background map was subtracted from the target image and replaced with that of the reference image. In the absence of seeing variations, or intrinsic source variability, the distribution of image flux deviations (measured within square pixel arrays, or super-pixels) with respect to the local background flux should be statistically the same between aligned image pairs. By plotting the two distributions against one another and determining the best linear fit, a simple linear flux correction can be made to the target image flux to correct for seeing changes. The super-pixels technique has the advantage of being empirically calibrated, avoiding strong assumptions on the form of the PSF. However in principle it is not as sensitive as difference imaging due to the potential loss of signal through binning flux into super-pixels.

Interestingly both of these methods separate out the background correction from the seeing correction. Modern difference imaging algorithms make these two corrections simultaneously. Whilst this is a highly efficient approach, as we shall show, it does not always yield optimal results.

### 2.2 Optimal image subtraction

Most difference image packages currently in use employ the Optimal Image Subtraction (OIS) algorithm presented by Alard & Lupton (1998) and generalized further by Alard (2000). In the OIS method a reference image  $R$  is convolved to match the PSF of a target image  $T$  that has been geometrically aligned and re-sampled to the same pixel grid as  $R$ . By taking into account differences in the background between  $R$  and  $T$  via a smooth 2D background model,  $B$ , the difference image,  $D$ , can be computed from linear least-squares minimization:

$$\sum_i D(x_i, y_i)^2 = \min \left\{ \sum_i [(R(x_i, y_i) \otimes K(u, v)) - T(x_i, y_i) + B(x_i, y_i)]^2 / \sigma(x_i, y_i)^2 \right\} \quad (1)$$

where  $(x, y)$  denote the position of image pixel  $i$ ,  $K$  is a kernel function that describes the PSF transformation between  $R$  and  $T$ ,  $(u, v)$  are coordinates centred on the kernel,  $\sigma^2$  is the pixel variance and  $\otimes$  denotes convolution. For computational efficiency Alard & Lupton (1998) advocate decomposing  $K$  into a linear combination of basis functions

$$K(u, v) = \sum_{k=1}^N \sum_{p,q=0}^{p+q \leq M_k} a_{pq} u^p v^q e^{-(u^2+v^2)/2\sigma_k^2}, \quad (2)$$

where  $a_{pq}$  are coefficients. The Gaussian widths  $\sigma_k$  and integers  $N$  and  $M_k$  control the complexity of the kernel shape. Similarly the differential background is modelled as a sum of polynomial basis functions:

$$B(x, y) = \sum_{r,s=0}^{r+s \leq M_b} a_{rs} x^r y^s, \quad (3)$$

where  $a_{rs}$  are coefficients and the integer  $M_b$  is the degree of polynomial used to model the differential background.

There are a number of freely available software implementations of the OIS algorithm, the best known of which are ISIS<sup>1</sup> and DIAPL<sup>2</sup>. Throughout this paper we use ISIS version 2.2 (Alard & Lupton 1998; Alard 2000). However, we stress that the shortcomings we illustrate are not specific to ISIS but are shared by all implementations of OIS that assume simple polynomial forms for the differential background as in Equation (3). As pointed out in the review of Wozniak (2008) the OIS method is actually independent of the choice of basis function. Bramich (2008) has implemented a version of OIS (DANDIA) in which Equation (1) is minimized pixel-by-pixel (i.e. essentially using a  $\delta$ -function kernel). This method solves for the kernel for an assumed constant background within a sub region. The global differential background solution is then found via interpolation over a grid of sub-regions. However for complex differential backgrounds of the kind investigated in this paper the method would potentially require splitting the image into a very large number of sub-regions in the absence of

<sup>1</sup> <http://www.iap.fr/users/alard/package.html>

<sup>2</sup> <http://users.camk.edu.pl/psych/DIAPL/>

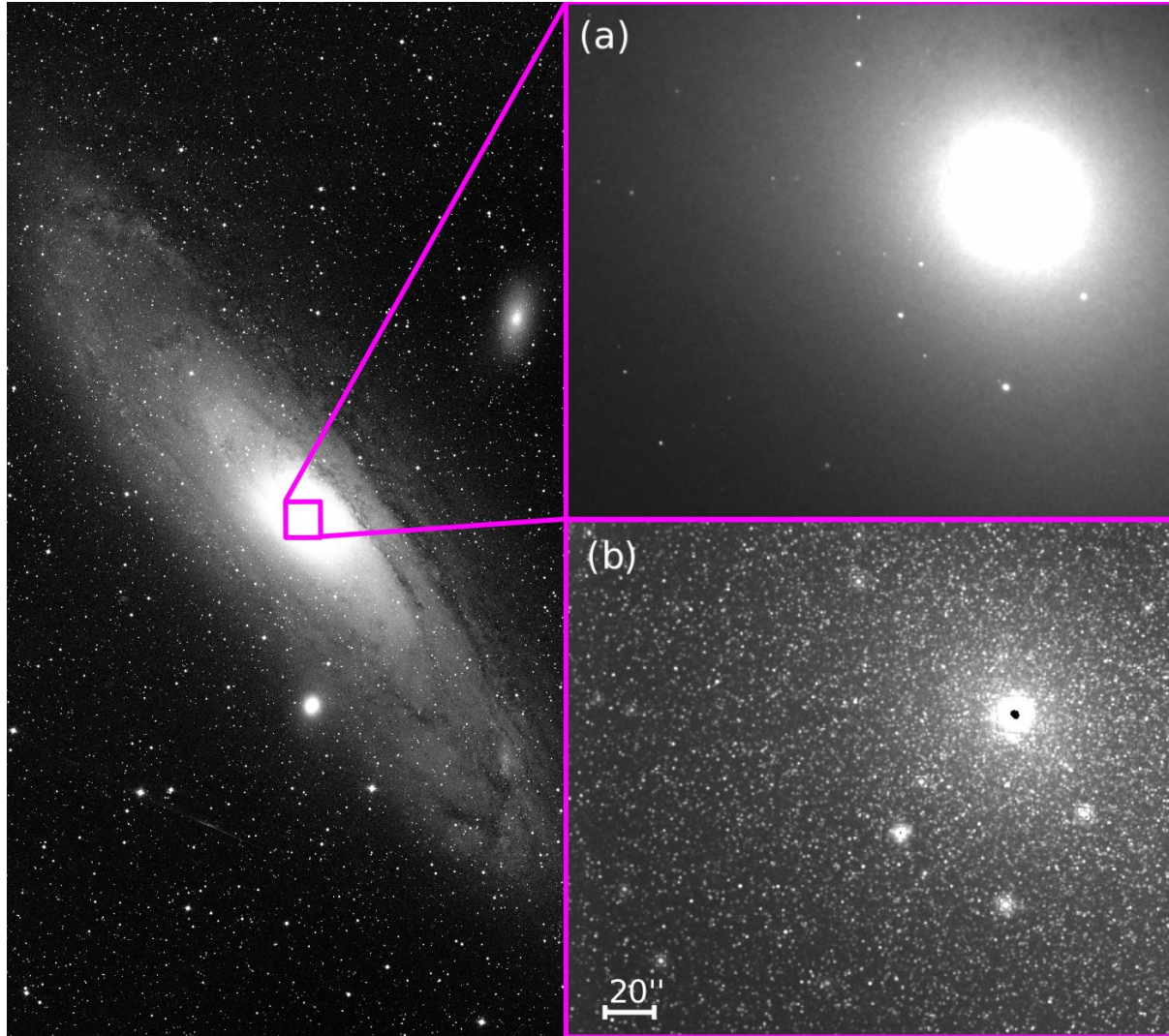


**Figure 1.** *Left panel:* The position of the Angstrom Project robotic field shown on an NOAO image of the Andromeda Galaxy (M31 - image credit: Bill Schoening, Vanessa Harvey/REU program/NOAO/AURA/NSF). *Right panels:* (a) A Sloan  $i'$ -band stacked image of the Angstrom Project robotic field obtained from the Liverpool Telescope at La Palma. This image is used as our reference image for the tests in this paper and covers the inner  $\sim 4' \times 4'$  of the M31 bulge. (b) The locations of thousands of variable stars around the M31 core are revealed by combining a stack of 480 difference images. The difference images span 5 years and are created from a sequence of more than 3300 individual exposures. The difference images were created using the modified method described in this paper. Composite residuals from imperfect subtraction within the inner  $\sim 10''$  of the core and around some bright foreground stars are also visible.

prior knowledge on the shape of the differential background and its behaviour with respect to time.

### 2.3 Difference imaging of Angstrom Project data

We have applied the OIS method to a series of Sloan  $i'$ -band images of the M31 bulge obtained by the Angstrom Project (Kerins et al. 2006) using the Liverpool Telescope (hereafter LT, Steele et al. 2004) on the Canary Islands. The Angstrom Project is undertaking long-term monitoring of the bulge of M31 in order to detect stellar microlensing events and transients. The survey employs a real-time difference imaging pipeline capable of issuing alerts of ongoing events (Darnley et al. 2007). The location of the Angstrom robotic telescope field is shown in Figure 1.

The LT is a 2m robotic telescope housing an optical camera (RATCAM) with a  $4'6 \times 4'6$  field of view with  $0''.13$  pixels. Im-

ages were obtained over a 5-year period from 2004–2009. The LT typically obtained one or two epochs of data per clear night during the M31 observing season (August–January) with each epoch comprising a run of between 7 and 15 short exposures, typically ranging from 30 to 200 seconds. The exposures were kept short to avoid saturation of the M31 core and bright foreground stars. Pre-processing, comprising de-biasing and flat fielding, was carried out by the LT robotic telescope pipeline. The Angstrom Project pipeline then performed preliminary geometric alignment and de-fringing, followed by optimal image alignment using Fourier cross correlation (for further details see Darnley et al. 2007). For the real-time pipeline the images are re-binned to  $1024 \times 1024$  pixels with a resolution of  $0''.26$ . In this paper we also use these re-binned images.

All images were built by aligning and stacking individual exposures within each observing epoch to form a high signal-to-noise

epoch frame. The master reference frame was constructed from a stack of 30 high quality individual exposures obtained over four separate epochs from the 2007/8 and 2008/9 observing seasons. These epochs were chosen on the basis of accurate telescope pointing and tracking, low airmass, low background levels and good seeing. ISIS can itself be used to build the reference image from a stack of high quality frames by matching their PSFs and background using Equation (1). We choose instead to create our reference frame by first photometrically aligning the selected images (using the method described in Section 3.1) and then median stacking them using the IRAF<sup>3</sup> IMCOMBINE task. Hence our difference image results rest only on a single application of Equation (1) when matching the reference and target images. The same reference image is used throughout so that variations in our results depend only on how we manipulate the target frame. The reference frame is shown in panel (a) of Figure 1.

Figure 2 shows some example difference images created from the reference image and a very high quality target image obtained under excellent seeing. The results illustrate the challenge of accurate background matching towards the core of M31 where, even within the small LT field of view, the dynamic range in surface brightness across the image is around two orders of magnitude. In Figure 2(a) ISIS uses a second-order polynomial to model the differential background across the whole image area. Whilst the resulting difference image clearly succeeds in revealing a wealth of variable stars (evidenced by the black and white spots, which show sources that have dimmed or brightened) it suffers from a significant large-scale background residual. We find that the amplitude of the residual is largely insensitive to the choice of polynomial order, though the residual pattern across the image does vary according to the order used, as one would expect. The underlying differential background is therefore clearly not well represented by a 2D polynomial. There are a number of possible causes for such an effect. Scattered light, internal reflections, dust and fringing effects can add localized unwanted flux contributions, whilst flat fielding errors may have a multiplicative effect. When observing a target like the M31 bulge which has a very bright and spatially varying background, the effects of such systematics are unlikely to be adequately modelled by a polynomial function.

In fact the amplitude of the background variation over most of the image area in Figure 2(a) typically represents only  $\lesssim 1\%$  of the original image flux, but this is still too large to allow reliable difference image photometry of sources, which themselves are varying at a level of a few percent of the background surface brightness flux. Since the residual background is epoch dependent the failure to effectively remove it means that robust relative photometry between epochs becomes virtually impossible. Additionally, the large-amplitude background residual may blunt the OIS algorithm's sensitivity to the optimal PSF transformation because the overall summed squared difference flux [ $D^2$  in Equation (1)] can become dominated by the background residual rather than by PSF kernel residuals.

Whilst these effects are important for high surface brightness regions such as the M31 bulge they are far less important for Galactic surveys that employ difference imaging. Even towards the Galactic bulge the flux observed by optical surveys is dominated

by resolved or semi-resolved stars and therefore any background residuals from systematic problems will be typically at a low level even on difference images. However, it is feasible that photometric corrections might benefit future near-infrared surveys of the Galactic bulge, which can target the centre of the Galaxy where the unresolved stellar background flux is considerably higher. Near-infrared array technology is also still maturing and so is currently more prone to systematic problems than optical CCDs.

The ISIS software also provides the option of running the OIS algorithm independently within sub-regions of an image. In Figure 2(b) we show the difference image result where ISIS has split the image into  $4 \times 4$  sub-regions. All other DIA parameters are the same as for Figure 2(a). This time ISIS does a better job over much of the image area. However, within the inner bulge region, covering around half the field area, noticeable background residuals are still evident, especially at the square sub-region boundaries, which show sharp discontinuity. One might be tempted to try to reduce the effect by further increasing the number of sub-regions. However, we are fundamentally limited by the size of the image stamps within which the convolution kernel is determined, which in turn is limited by the scale of the image PSF. For the image in Figure 2(b) each sub-region is only around 200 pixels wide, compared to a stamp width of 30 pixels. Ideally the PSF and background should be evaluated within several independent stamps across the sub-region in order to facilitate a good solution for the PSF transformation. The sub-regions also should be large enough to contain resolved or partially resolved stars, or strong features such as dust lanes, so that the solution to equation (1) is not dominated by noise.

These limitations force us to consider treating the differential background matching separately from PSF matching.

### 3 A MODIFIED PROCEDURE FOR DIFFERENCE IMAGING

We have seen towards high surface brightness targets such as M31 systematic effects such as scattered or reflected light can imprint complex time-variable signatures upon the differential background that the OIS algorithm cannot deal with adequately. The OIS algorithm performs PSF and background flux matching simultaneously, whilst prior to OIS these were treated separately by various M31 variable photometry pipelines (Tomaney & Crotts 1996; Ansari et al. 1997). However, the OIS algorithm provides clear advantages over earlier schemes due to its flexibility in modelling the PSF. Ideally we would like to combine the best of the old and current approaches.

To this end we choose to separate out the photometric and PSF matching stages, as in earlier approaches. Then we run ISIS with differential background matching effectively turned off by setting the background polynomial to order zero [i.e. setting  $M_b = 0$  in Equation (3)]. In this case the least squares minimization of  $D^2$  in Equation (1) should be driven by the quality of the PSF transformation kernel  $K$  rather than potentially having to trade between the quality of PSF and background matching.

#### 3.1 Photometric alignment

We begin by determining a gross linear photometric scaling to match the image flux. Due to large telescope pointing errors in the first two seasons of the Angstrom survey the sky area common to all exposures represents less than half the available image area. We therefore use the largest available rectangular region common to

<sup>3</sup> IRAF is distributed by the National Optical Astronomy Observatories, which are operated by the Association of Universities for Research in Astronomy, Inc., under cooperative agreement with the National Science Foundation.



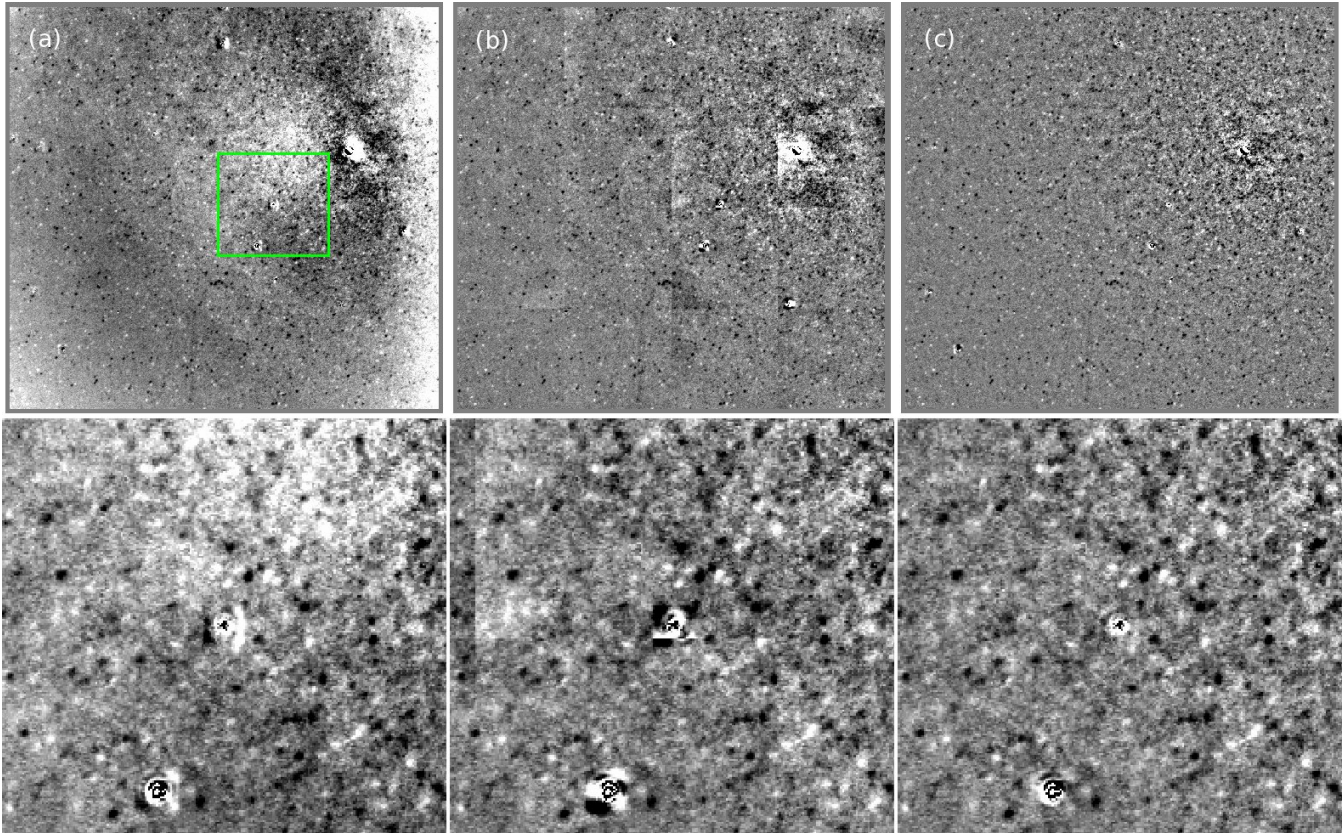


**Figure 2.** *Upper panels:* difference images produced by ISIS (version 2.2) from a pair of high quality reference and target images covering an area of  $3'.9 \times 3'.7$  around the M31 core. In (a) ISIS is run on photometrically unaligned images allowing a second-order polynomial to model the differential background. Strong background residuals remain in the difference image, which do not markedly improve with the use of higher order polynomials. In (b) the photometrically unaligned images are split into 16 sub-regions on which ISIS is run individually using the same parameters as in (a). The background matching is better further out from the core (apparently at the expense of poorer PSF matching) but remains poor closer to the core where the boundaries between the sub-regions are evident. In (c) the images have been photometrically aligned using the method discussed in this paper, prior to running ISIS. In this case a zeroth-order polynomial has been imposed for the differential background when running ISIS. All other parameters are the same as in (a) and (b). *Lower panels:* show a  $1' \times 0'.9$  zoom of the region shown by the box in (a) for each case (a), (b) and (c), respectively. In (c) note how the removal of the differential background also improves the quality of PSF matching as evidenced by the lessened residuals around bright foreground stars.

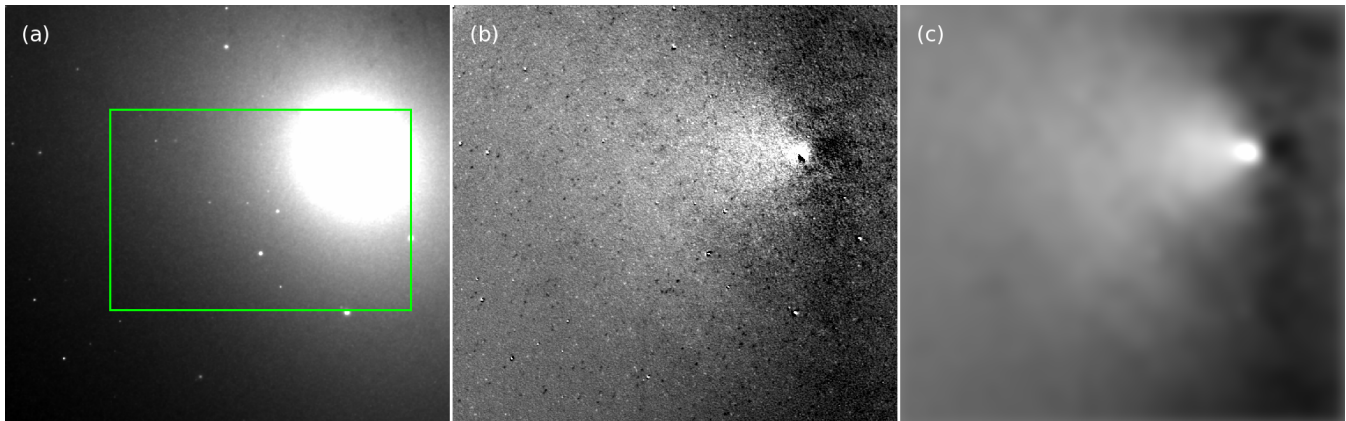


**Figure 3.** Matching the non-linear background residual. A target image (a) is linearly matched to the reference image [shown in Figure 1(a)] via a fit to the pixels within the rectangular boundary, a region common to all exposures. The resulting linearly aligned image is then directly subtracted from the reference to reveal a residual map (b). The map reveals a large scale non-linear variation in the residual background level. This map is then Gaussian filtered to produce a smoothed residual background map (c). The contrast level in (b) and (c) has been stretched by a factor 30 over that in (a) to highlight the background residual, which has an amplitude that is typically only about 1% of the target image flux. The smoothed residual map is added back on to the target image to produce the final photometrically corrected target frame. The difference image resulting from the corrected target frame is shown in Figure 2(c).

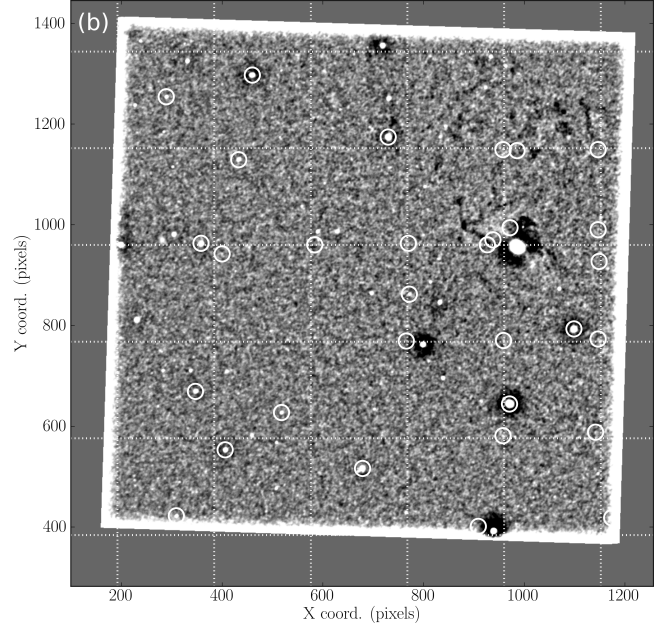
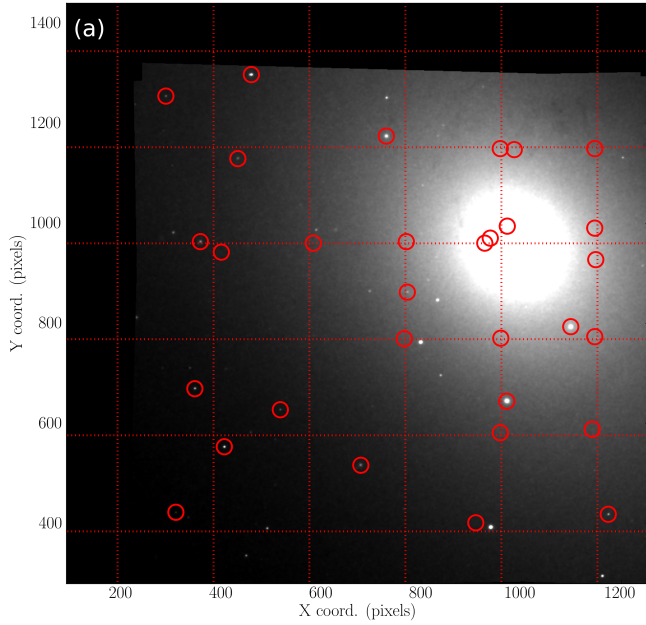


**Figure 5.** The reference image and target “structure map” aligned to the same global pixel coordinates. (a) The reference image, showing the locations of 31 objects (shown circled - mostly foreground stars or features relating to dust lanes) selected by ISIS to determine the convolution kernel. One object is selected within each of the square sub-regions which form an overlapping mesh indicated by the dotted lines. In (b) we show a noise-normalised map of residual structure in the target image. The structure map is formed by subtracting a smoothed version of the target and then dividing the result by the square-root of the target flux. Foreground stars show up clearly on the structure map, as do dust lanes close to the M31 core and in the upper right of the image. The granular structure in the image is not noise but partially resolved bright stars and unresolved clumps of stars in M31. The smoothing aperture produces the dark ringing effect evident around some of the brighter foreground stars and the M31 core, as well as the border around the image perimeter.

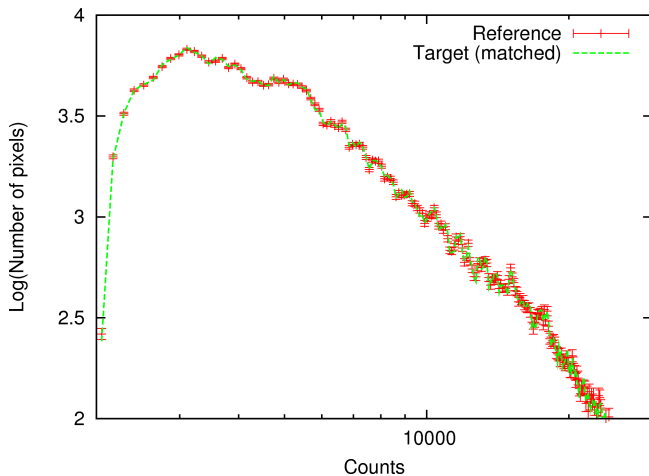


**Figure 4.** Flux count histograms of the reference image (points with errors) and target image (dashed line) after the target has been photometrically aligned to the reference. The pseudo errors on the reference image pixel numbers assume an expected Poisson-like variance in the pixel numbers between aligned images. After alignment the behaviour of the target count histogram accurately mirrors that of the reference image even down to small scale deviations.

all images, which covers around 30% of the image area (see Figure 3) in order to photometrically align our images. We determine a gross linear scaling and offset between the reference  $R$  and target  $T$  ( $R = a \times T + b$ ) using the LINMATCH task within IRAF. The scaling  $a$  and offset  $b$  are then applied to  $T$  to obtain a linearly pho-

tometrically matched image  $T_L$ . After linear scaling we subtract  $T_L$  from  $R$  to obtain a residual image  $R - T_L$ . Since the seeing is generally different between  $R$  and  $T_L$  the differential flux from genuinely variable sources is significantly smoothed out by differences in image PSF. A Gaussian filter is then passed over the residual image to produce a smoothed residual background image  $B'$ . The size of the Gaussian is set to  $\sigma = 15$  pixels, which is large enough to be insensitive to the presence of variable stars but small enough to provide a good local estimate of the differential background. Finally a background corrected target image  $T' = T_L + B'$  is obtained. Figure 3 illustrates how the differential background map  $B'$  is produced from a target image which has already been linearly matched to the reference frame.

Figure 4 shows the resulting pixel flux histograms after photometric matching. Around the M31 bulge the image flux is dominated almost everywhere by the smooth unresolved surface brightness distribution, so the photometric calibration is insensitive to seeing and we are able to obtain very good photometric alignment without the need for PSF corrections.

The adjusted image  $T'$  now has a background that is properly matched to  $R$  so that ISIS can be run without the inclusion of the  $B$  term in Equation (1). Note that this matching is effective only against systematic effects which are additive (e.g. scattered light). One might imagine that a poorly constructed flat field could cause a non-uniform multiplicative variation across the image, in which case the method described here would not adequately correct the flux.



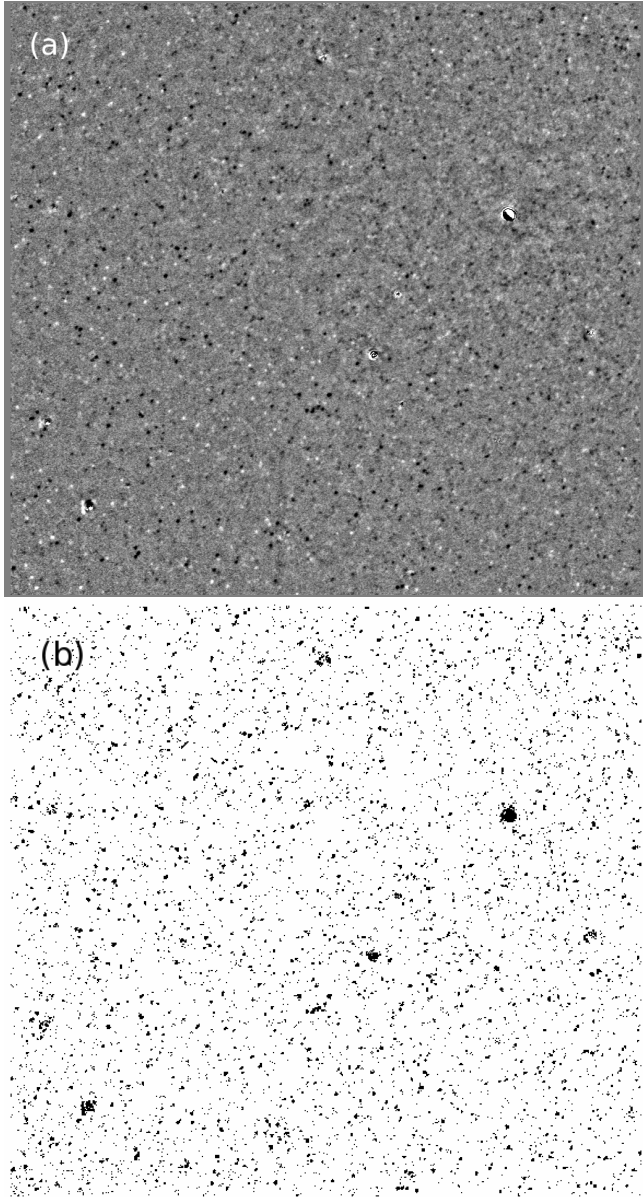


**Figure 6.** (a) Grey-scale “signal-to-noise” map produced by dividing the difference image shown in Figure 2(c) by the square root of the combined reference and target image counts. Note how the increase in image noise towards the M31 core suppresses the number of detectable variations there (compare the contrast of sources close to the core with those further out) though some are still evident to within  $\sim 10''$  of the core. (b) A map of all the pixels in (a) that exceed  $2.5\sigma$ . Isolated random noise pixels are comparatively rare and most belong to PSF-like clusters that are associated with genuinely variable objects. These provide the excess seen in the tails of the noise histogram shown in Figure 7.

### 3.2 PSF matching and difference image results

Before running ISIS on our photometrically aligned data we make checks on whether there is enough information on the PSF within our images for ISIS to make a reliable PSF kernel determination. Since the surface brightness of the M31 bulge is high the number of obvious resolved stars is relatively small.

ISIS determines the PSF kernel transformation not by using all the image pixels but by sampling the image within a number

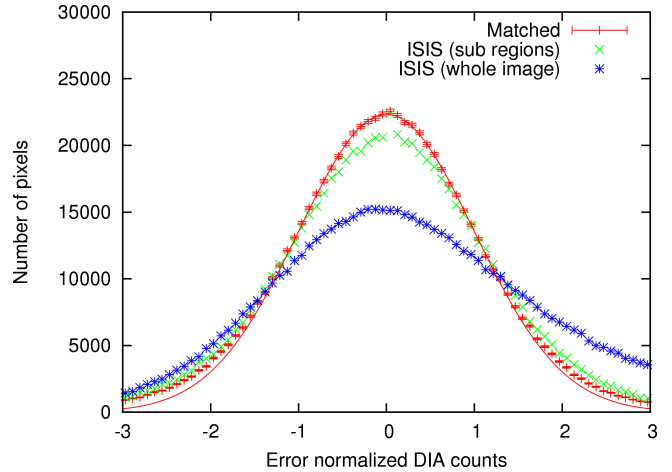


**Figure 7.** Histogram of the counts for the image shown in Figure 6(a) together with a unit-width Gaussian model. The amplitude of the Gaussian is fitted to data points within  $\pm 1\sigma$ . The excess from pure Gaussian noise evident in the tails of the histogram is predominately associated with genuinely variable objects as shown in Figure 6. Also shown are the equivalent histograms for the difference images shown in Figure 2(a) and (b) where no photometric alignment is performed prior to running ISIS.

of small regions (“stamps”) dispersed over the image. The location of the stamps can be partly constrained by the user specifying a grid of sub-regions. ISIS determines the most suitable stamp location within each sub-region, usually centring the stamp on a bright star. The quality of the PSF transformation is therefore partly determined by the number of user-defined sub-regions and by the success with which ISIS finds suitable stamps within each sub-region.

Figure 5 shows the reference image (a) and “structure map” of our test target image (b) on which is over-plotted the sub-region grid adopted for the tests in this paper. The structure map is produced by subtracting a Gaussian smoothed version of the target image from the original target frame and then dividing the result by the square root of the target pixel flux. This removes the smooth background light component of the M31 surface brightness, clearly revealing foreground Milky Way stars as well as dust lanes, semi-resolved bright stars and stellar clumps in M31 itself. The structure map clearly shows that there is a wealth of structure over the whole image area which is potentially useful for PSF determination.

The grid overlay in Figure 5(a) and (b) is defined with respect to a  $1536 \times 1536$  pixel area which defines a global pixel coordinate system onto which all images have been aligned. (The large relative size of this area is necessitated by large pointing offsets in some of the earlier exposures.) The circles in Figure 5(a) and (b) indicate the locations of the centre of each of 31 stamps which ISIS selected for our test target frame. We set the size of each stamp to  $30 \times 30$  pixels, so that collectively the stamps comprise about 3% of the available image area. More often than not the stamps are centred on bright foreground stars, however it is clear from Figure 5 that a number of the stamps are not centred on any obvious star. We find that the steep surface brightness gradient is a strong determinant as to whether the ISIS stamp finding algorithm locates a bright star or not.

In order to determine the PSF kernel reliably, the number of stamps should be at least  $3(1 + M_k)(2 + M_k)/2$  (Alard & Lupton 1998; Alard 2000), where  $M_k$  is the user-specified polynomial order allowed for the spatial variation of the kernel (see Equation 2). For our data we find  $M_k = 1$  sufficient to characterise spatial PSF

kernel variations, so that we require a minimum of 9 good stamps. In fact, typically the ISIS stamp finding algorithm results in  $\sim 15$  stamps centred on genuine bright foreground stars, more than sufficient to compute a reliable kernel. We have also checked that using an improved star finding algorithm, in which all the stamps are centred on obvious stars, makes little difference to the overall difference image result. In fact, whilst the bright foreground stars are preferred for PSF determination, the granular structure of partially resolved M31 stars evident in Figure 5(b) means that just about any position on the image will provide some useful information for the PSF kernel determination. We therefore proceed with the default stamp finding algorithm which is contained in the ISIS package.

The result of running ISIS on a target image that is now photometrically aligned to the reference frame is shown in Figure 2(c). All ISIS configuration parameters are set the same as for the previous tests in Figure 2(a) and (b) except we now enforce a zeroth-order polynomial model for the differential background. The resulting difference image is clearly superior to the previous examples. There is now no noticeable background residual anywhere on the image. Equally important is the fact that the PSF transformation is clearly much improved too. This is evident when examining the residuals associated with the few bright foreground stars visible within the Angstrom field (compare with the reference image shown in Figure 1). These foreground stars leave relatively strong residuals in the difference images shown in Figure 2(a) and (b) but they are much reduced in Figure 2(c) (see also the zoomed inset panels). This indicates that ISIS has been able to find a better PSF solution as a result of minimizing Equation (1) for photometrically aligned images.

Figure 6(a) shows a map of the signal to noise ( $S/N$ ) ratio. The signal-to-noise map is defined by

$$S/N = \frac{\sqrt{gMN}(R - T)}{\sqrt{MT + NR}}, \quad (4)$$

where  $M$  is the number of individual exposures comprising the target frame stack  $T$ ,  $N$  is the number of individual exposures comprising the reference stack  $R$  and  $g$  is the CCD gain. The grey-scale in Figure 6(a) is calibrated to show pixels with  $|S/N| > 10$  as either white or black depending upon whether the difference flux is positive or negative. The main difference in the appearance of this  $S/N$  image with the corresponding difference image shown in Figure 2(c) is that near the M31 core the  $S/N$  image shows much less variation, indicating that many of the flux deviations on the difference image near the M31 core are just due to the noise arising from the very high surface brightness level. Figure 7 shows the resulting pixel histogram of  $S/N$  values for the photometrically aligned target frame and for the unaligned cases shown in Figure 2(a) and (b). These histograms demonstrate a clear improvement both in the symmetry and width of the noise distribution as a result of carrying out separate photometric alignment. Over-plotted on the noise histogram of the aligned data is a unit-width Gaussian model, where the amplitude has been fitted within  $\pm 1\sigma$ . The histogram shows that within this region the noise is well approximated as Gaussian. Towards the tails of the distribution there is an excess over and above Gaussian noise. However, as shown in Figure 6(a) and (b), this excess is associated with genuinely varying objects which make up a non-negligible fraction of the image pixels. Figures 6 and 7 therefore suggest that photometrically aligned images can allow high quality difference imaging even to within a few arcseconds of the M31 bulge.

### 3.3 The effect of variables

The high crowding levels of genuinely variable sources evident in Figure 2 potentially poses a problem for the OIS algorithm. The minimization in Equation (1) would be expected to correspond to the optimal difference image only in the limit that, in the absence of seeing and background variations, most of the image flux does not vary with time. In theory it could be the case that the relative phases and amplitudes of variables within a stamp at a given epoch could pose a significant source of time variability in the average difference flux within the stamp. If so this could also affect the residual background model determination.

In order to suppress the effects of genuine variations on the computed kernel ISIS uses sigma clipping both of pixel values within stamps and of the distribution of stamps themselves. However, for the M31 bulge, where a relatively high fraction of pixels change due to astrophysical variation, sigma clipping can lead to a significant fraction of the image area being excluded, particularly around the M31 core.

To test the potential impact of the high sky density of variables we perform a double-pass iterative minimization of Equation (1) that corrects the target image for the presence of variable sources. On the first pass ISIS is run in the normal way. Then, all pixel fluxes on the resulting difference image above a specified absolute flux threshold are added back on to the target frame to form a modified target image in which intrinsically variable sources are largely removed (i.e. matched to their flux values on the reference image). A second pass of ISIS is then performed on this modified target frame. The resulting kernel solution for the modified frame is then applied to the reference image and the convolved reference is subtracted from the original (unmodified) target frame to create the final difference image. This method ensures that the final difference image is largely insensitive to the presence of variable stars and that as much of the image area as possible is used to compute the kernel.

Reassuringly, we find virtually identical results are recovered using either a standard ISIS run or the double-pass method described above, showing that ISIS is capable of finding an optimal kernel solution even for high crowding densities of variable stars.

## 4 EXAMPLE LIGHT-CURVES

In Figures 8 and 9 we show two periodic variable star light-curves from the Angstrom Project data processed with and without the photometric alignment stage described in Section 3.1. Figure 8 shows the light-curve of a variable with a period of 501 days located  $2'.4$  from the M31 core monitored over five observing seasons. The right-hand and left-hand columns show the results with and without photometric alignment, respectively. Panel (a) shows the light-curve itself, panel (b) is the computed periodogram, and panel (c) is the result of folding the light-curve with the period corresponding to the peak in the periodogram.

Looking at panel (a) in the right-hand column of Figure 8 we see that the light-curve derived from the photometrically aligned images appears much more coherent and less scattered than that derived from unaligned data in the left-hand panel. Panel (b) shows the computed periodogram for periods from 5 to 5000 days calculated using the Generalised Lomb Scargle method of Zechmeister & Kürster (2009). This generalised method extends the standard Lomb Scargle approach by taking account of errors on the flux and not assuming a zero mean flux, making the periodogram computation more reliable when there are large time gaps in the data

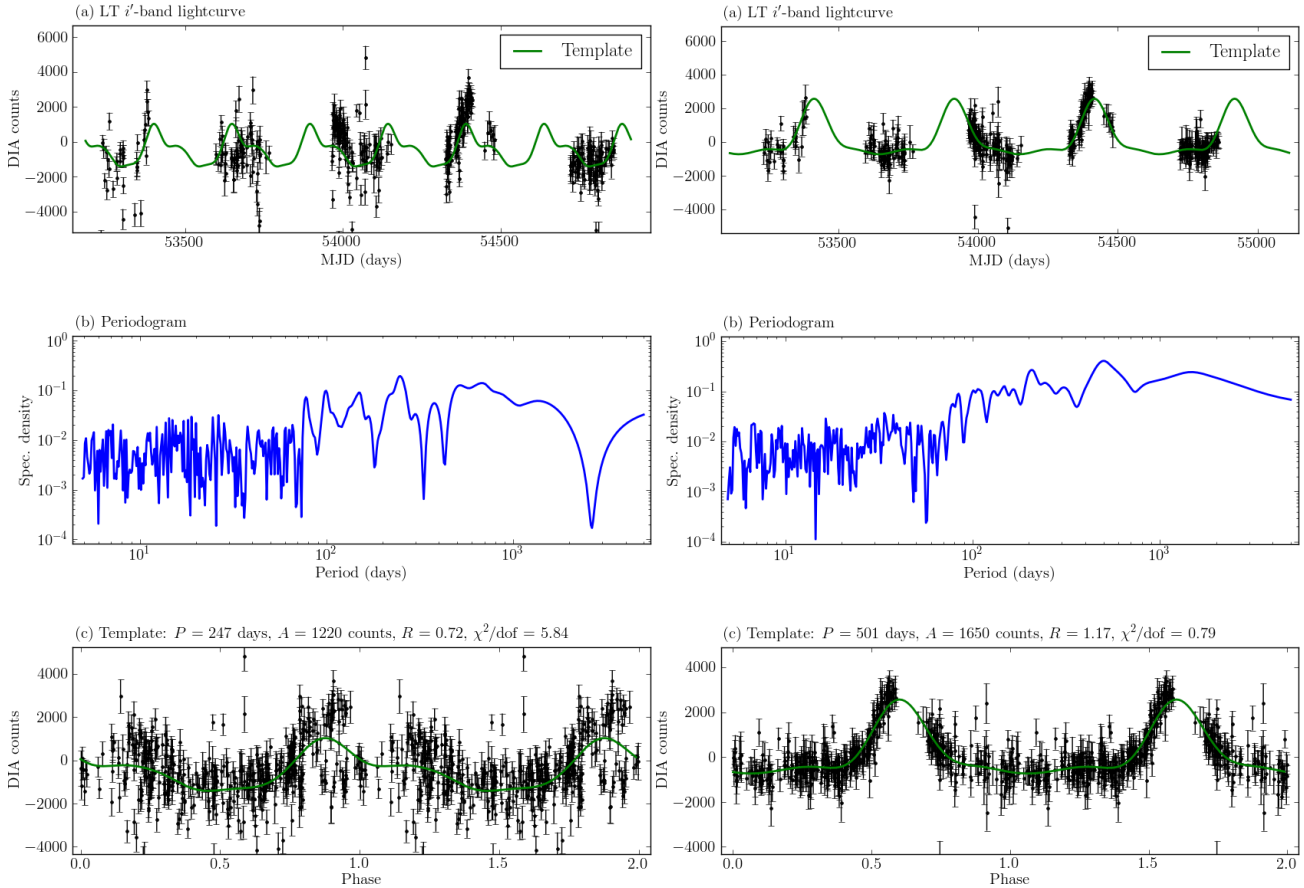


**Figure 8.** A five-season LT  $i'$ -band light-curve of a periodic variable star located  $2\frac{1}{4}$  from the M31 core. Results using ISIS applied to photometrically unaligned images are shown in the left-hand column whilst those from aligned images are shown in the right-hand column. In each case panel (a) shows the light-curve, panel (b) shows the spectral density computed using the Generalised Lomb Scargle method of Zechmeister & Kürster (2009) and panel (c) shows the result of folding the light-curve in (a) by the period corresponding to the maximum in the spectral density shown in (b). A smoothed light-curve template constructed using radial basis function interpolation (see main text) of the folded light-curve is indicated by the smooth curve in (a) and (c). In (c) the folding period  $P$ , the variable half amplitude  $A$ , the asymmetry ratio  $R$  and the reduced  $\chi^2$  with respect to the template curve (excluding the 6 worst outlying points) are also given. The asymmetry ratio  $R$  is the ratio of the rise (minimum up to peak) and fall (peak back to minimum) time-scales, as determined from the smooth template. Note how in the unaligned case the systematic scatter has resulted in an incorrect period determination.

(such as for seasonal surveys like ours). The period corresponding to the peak in the spectral density is used to fold the light-curve data in panel (c). The folded data in the right-hand column clearly exhibits well defined periodic behaviour.

In order to provide a guide on the performance of the photometry we compute the reduced  $\chi^2$  with respect to model templates of the light-curve behaviour. We assume the underlying behaviour of the folded data to be smooth on temporal scales much larger than the time resolution of the folded data. This may not always be the case so the resulting  $\chi^2$  assessment should be conservative in the sense of not being an over-optimistic indicator of the true performance. We construct a template for each light-curve using the SciPy<sup>4</sup> implementation of the multiquadric radial basis function (RBF) approximation, which is a generalisation to the case of noisy data of multiquadric RBF interpolation (Hardy 1971). The RBF approximation is controlled by two parameters: a shape parameter ( $\epsilon$ ) and a smoothness parameter ( $S$ ). The shape parameter controls the way in which the interpolation function weighting varies with Euclidean distance (norm) from the data points, whilst the smoothness

parameter controls the level of smoothing over scatter in the data. Setting  $S = 0$  would be equivalent to strict interpolation, where the template is forced through every data point (clearly inappropriate for noisy data). We fix these parameters throughout at  $\epsilon = 0.25$  and  $S = 0.05$  which, for adequately sampled light-curves, provide a good description of trends in light-curve behaviour without appearing to over-fit the data; light-curve “structure” below  $\sim 1/4$  of a phase is typically unresolved. For the computation of the multiquadric RBF approximation it is desirable to first rescale the flux axis so that both the flux and phase axes have similar numeric scales (of order unity). This ensures that the interpolation weighting is sensitive to displacements along both axes.

Looking at the left-hand panels of Figure 8 we see that the systematic scatter in the light-curve derived from photometrically unaligned data results in a significantly distorted periodogram which peaks at the wrong period. Since for our DIA testing we have not attempted to exclude poor quality images the light-curves all contain a small number of obvious outliers. When computing the reduced  $\chi^2$  with respect to the RBF template we therefore exclude the 6 worst outlying points (representing 1.25% of the full dataset) in order to obtain a fair measure of how well the template represents the bulk of the data. The reduced  $\chi^2$  value reported in panel (c) is quite

<sup>4</sup> <http://www.scipy.org/>



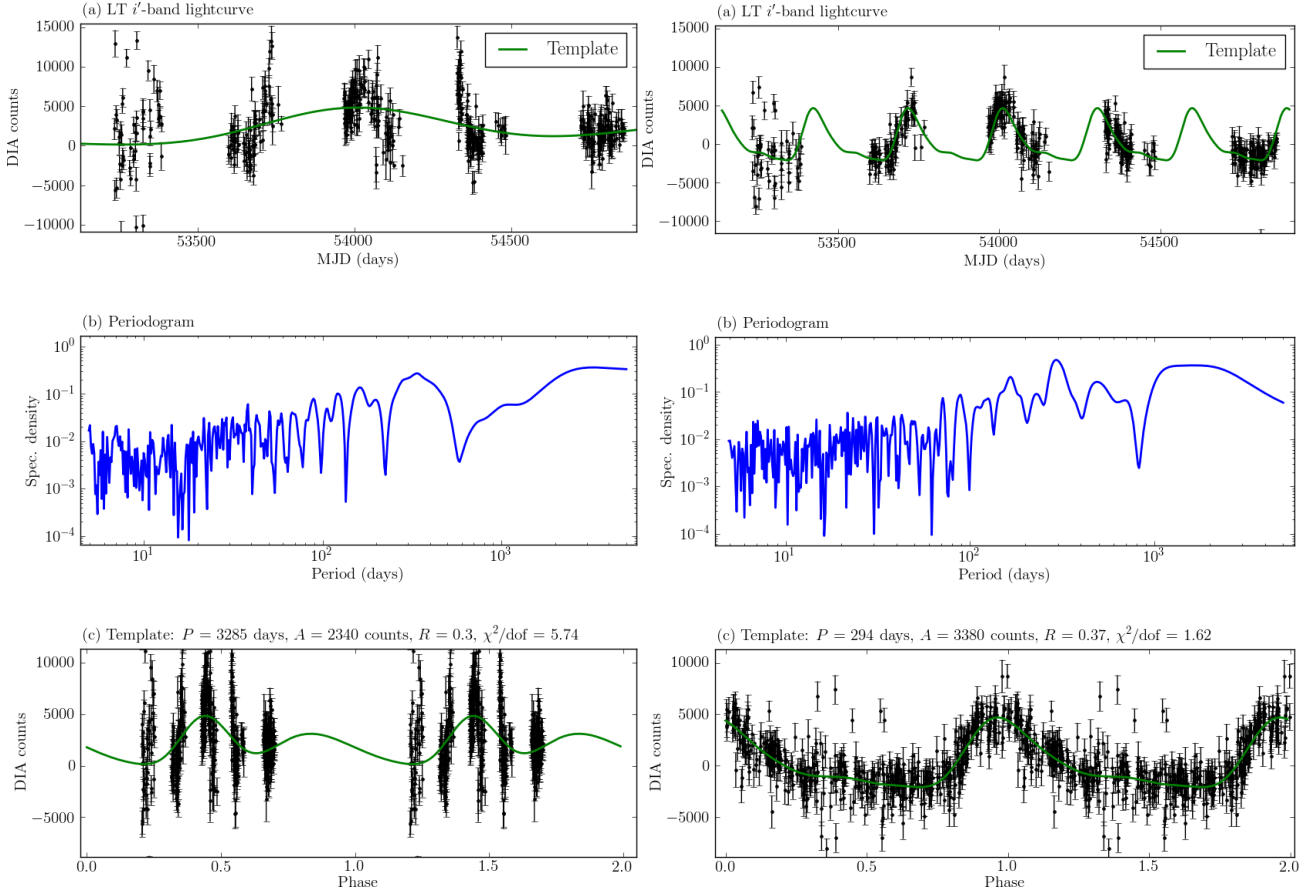


**Figure 9.** As for Figure 8 but this time for a variable star located just  $19''$  from the M31 core. In the unaligned case displayed in the left-hand column the periodogram fails to identify the correct period and instead the peak spectral density reflects merely the season-to-season variation in average flux.

acceptable for the aligned data but clearly poor for the unaligned folded dataset.

Figure 9 shows a similar situation for a variable star with a period of 294 days located just 19 arcsec from the M31 core, corresponding to a projected distance from the core of just 72 pc for an M31 distance of 780 kpc. In the unaligned case the peak in the periodogram is completely spurious, corresponding to the seasonal variation in average flux due to different parts of the variable phase being sampled in different observing seasons. Once again the reduced  $\chi^2$  for the RBF template is quite acceptable for the light-curve derived from aligned data but poor for the unaligned dataset. The examples of Figures 8 and 9 show that careful photometric alignment is essential for the accurate characterisation of variable signals.

It is noticeable that the first season of Angstrom data shows good consistency with subsequent seasons for the variable star shown in the right-hand column of Figure 8, which is located  $2.4''$  from the M31 core (about a half of the LT field width away). However the light-curve of the variable close to the M31 core shown in the right-hand column of Figure 9 is much more erratic during the first season than in subsequent seasons. Visual inspection of the images shows that the majority of images taken during the LT commissioning season in 2004 show evidence of scattered or reflected light close to the core. Improvements in light baffling made to the LT in early 2005 substantially improved the quality of later data.

Figure 10 shows six more examples of detected variable stars at angular distances from the M31 core ranging from 223 arcsec

(near the edge of our reference field) down to just 9 arcsec. They illustrate good season-to-season consistency in the corrected photometry, as evidenced by the smooth continuity of the folded light-curve, and also reasonable characterisation of the noise, as indicated by the size of the reduced  $\chi^2$  values with respect to the RBF template.

The variable in Figure 10 located at 9 arcsec from the core has a predictably very noisy light-curve and is at the threshold of detectability; whilst it displays clear periodic behaviour the structure of the variation is not well resolved due to noise. We therefore determine that the technique works well at least beyond  $\sim 10$  arcsec from the M31 core. As Figure 6 shows, there are relatively few variable objects that are detectable above the noise so close to the M31 core but the examples in Figures 9 and 10 demonstrate that, where they are detectable, we are usually able to obtain reliable photometry even in this extreme high-background regime.

## 5 DISCUSSION

In this paper we have shown that optimal difference imaging in regions of very high background levels, such as the bulge regions of galaxies, can be severely compromised due to the presence of systematics such as internal reflections, scattered light, or fringe effects. In these cases difference images created using the Optimal Image Subtraction (OIS) algorithm (Alard & Lupton 1998; Alard 2000), which is the most widely used difference image algorithm,

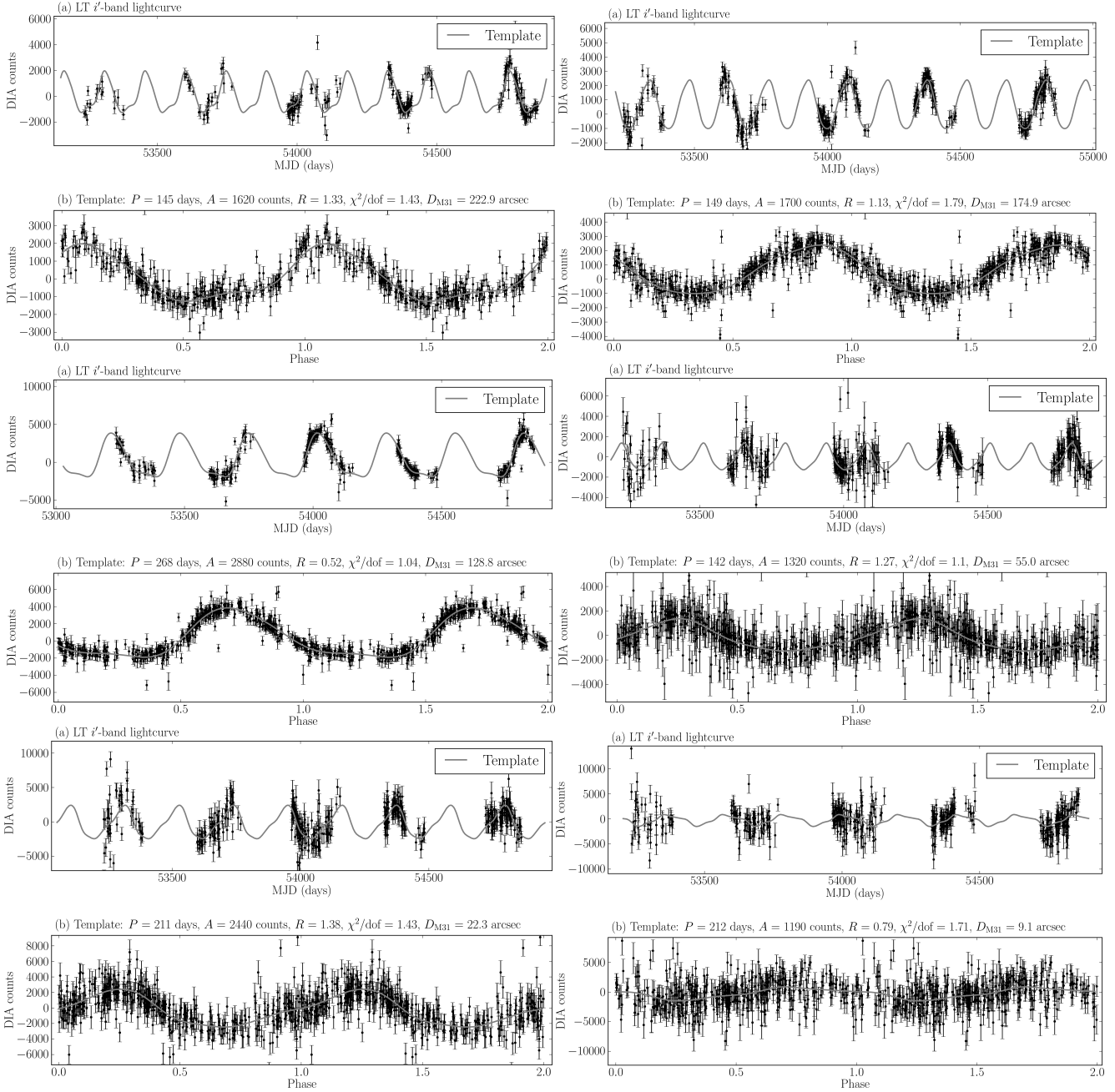


**Figure 10.** Corrected light-curves for a sample of six periodic variable stars over a range of distance from the M31 core. The five-season light-curves are shown in the panels labelled (a) together with the smooth template determined from the folded light-curve. The folded data is shown in panel (b) below each light-curve. The statistics displayed above the folded data is as for Figures 8 and 9, with the addition of  $D_{\text{M31}}$  which is the angular distance of the object from the M31 core in arcseconds.

may exhibit large amplitude background residuals that make reliable relative photometry difficult if not impossible. Fortunately, we have shown that OIS is able to give very good results provided the images to be differenced are first photometrically aligned prior to difference imaging.

Using the photometric alignment procedure described in this paper we find we can produce difference images of the M31 bulge that are close to photon noise limited. Not only does it minimize or eliminate large amplitude background residuals but it also noticeably improves the quality of the PSF kernel transformation. We have tested the modified pipeline by producing several examples of

periodic variable light-curves from the Angstrom Project survey of the M31 bulge. The results allow characterisation of periodic signals even to within  $\sim 10$  arcseconds of the M31 nucleus.

The problem we highlight is specific to targets in which the background brightness is high and subject to systematic variations which have complex spatial signatures. The OIS method is well known to cope admirably for stellar fields within our Galaxy, as imaged by current optical surveys, where the image flux is dominated by resolved or semi-resolved stars rather than by the diffuse background light. However, future near-infrared time-domain sur-

veys of the Galactic Centre could also conceivably benefit from a separation of the photometric and kernel matching stages.

## ACKNOWLEDGEMENTS

It is a pleasure to thank the referee, Przemyslaw Wozniak, for many useful suggestions which helped to improve this paper. JPD was supported by a PhD studentship from the UK Science and Technology Facilities Council (STFC). This work was supported by the research grant of the Chungbuk National University in 2009. The Liverpool Telescope is operated on the island of La Palma by Liverpool John Moores University in the Spanish Observatorio del Roque de los Muchachos of the Instituto de Astrofísica de Canarias with financial support from STFC.

## REFERENCES

- Alard, C. & Lupton, R., 1998, *ApJ*, 503, 325  
 Ansari R., et al., 1997, *A&A*, 324, 843  
 Alard, C. 2000, *A&AS*, 144, 363  
 Bramich, D. M. 2008, *MNRAS*, 386, L77  
 Darnley, M. J., et al. 2007, *ApJ*, 661, L45  
 Hardy, R.L., 1971, *J. Geophys. Research*, 76, 1905  
 Kerins, E., Darnley, M. J., Duke, J. P., Gould, A., Han, C., Jeon, Y.-B., Newsam, A., & Park, B.-G. 2006, *MNRAS*, 365, 1099  
 Steele I. A., et al., 2004, *SPIE*, 5489, 679  
 Tomaney, A. B., & Crotts, A. P. S. 1996, *AJ*, 112, 2872  
 Wozniak, P. 2008, Manchester Microlensing Conference, eds E. Kerins, S. Mao, N. Rattenbury and L. Wyrzykowski, Published online at SISSA, Proceedings of Science, p.3  
 Zechmeister M., Kürster M., 2009, *A&A*, 496, 577